

# In-Cylinder LIF Imaging, IR-Absorption Point Measurements, and a CFD Simulation to Evaluate Mixture Formation in a CNG-Fueled Engine

**Patrick Kranz, Daniel Fuhrmann, Martin Goschütz, and Sebastian A. Kaiser, University of Duisburg-Essen, Germany**  
**Stephan Bauke, Kai Golibrzuch, and Hainer Wackerbarth, Laser-Laboratorium Göttingen eV, Germany**  
**Peter Kawelke, Julian Luciani, Lars Beckmann, and Jasper Zachow, Volkswagen AG, Germany**  
**Manuel Schütte, Olaf Thiele, and Thomas Berg, LaVision GmbH, Germany**

## Abstract

Two optical techniques were developed and combined with a CFD simulation to obtain spatio-temporally resolved information on air/fuel mixing in the cylinder of a methane-fueled, fired, optically accessible engine. Laser-induced fluorescence (LIF) of anisole (methoxybenzene), vaporized in trace amounts into the gaseous fuel upstream of the injector, was captured by a two-camera system, providing one instantaneous image of the air/fuel ratio per cycle. Broadband infrared (IR) absorption by the methane fuel itself was measured in a small probe volume via a spark-plug integrated sensor, yielding time-resolved quasi-point information at kHz-rates. The simulation was based on the Reynolds-averaged Navier-Stokes (RANS) approach with the two-equation k-epsilon turbulence model in a finite volume discretization scheme and included the port-fuel injection event. Commercial CFD software was used to perform engine simulations close to the experimental conditions. Experimentally, the local gas temperature influences both LIF and IR measurements through the photophysics of fluorescence and IR absorption, respectively. Thus, in advances over previous implementations, both techniques also measured temperature and used this information to improve the accuracy of the measured air/fuel ratio. In the vicinity of the IR sensor, the local temperature deviated significantly from the bulk-gas temperature due to heat transfer. This was consistent with results of LIF measurements and CFD simulation. The simultaneous application of the two different, but complementary optical techniques together with a simulation gave detailed insight into mixture formation in the port-fueled engine. It also allowed for a cross-check of the uncertainties associated with the experiments as well as the simulation.

## History

Received: 15 Mar 2018  
Accepted: 10 Apr 2018  
e-Available: 28 Dec 2018

## Keywords

Optical diagnostics, Laser-induced fluorescence imaging, LIF thermometry, Infrared absorption measurement, CFD simulation, Compressed natural gas, Methane, Anisole, Port-fuel injection, Optical engine

## Citation

Kranz, P., Fuhrmann, D., Goschütz, M., Kaiser, S. et al., "In-Cylinder LIF Imaging, IR-Absorption Point Measurements, and a CFD Simulation to Evaluate Mixture Formation in a CNG-Fueled Engine," *SAE Int. J. Engines* 11(6):1221-1238, 2018, doi:10.4271/2018-01-0633.

ISSN: 1946-3936  
e-ISSN: 1946-3944



© 2018 LaVision GmbH; Published by SAE International. This Open Access article is published under the terms of the Creative Commons Attribution License (<http://creativecommons.org/licenses/by/4.0/>), which permits use, distribution, and reproduction in any medium, provided that the original author(s) and the source are credited.

This article is based on a presentation at WCX18, Detroit, MI, April 10-12, 2018.



## Introduction

Air/fuel mixing in internal combustion (IC) engines affects ignition, combustion, and pollutant formation. Not only in spark-ignited (SI) direct-injection (DI) engines, but even in engines with port-fuel injection (PFI), the injection parameters influence mixture formation in the cylinder and the mixture may not be homogeneous at ignition. Therefore, much previous work has investigated air/fuel mixing. Experimentally, laser-based imaging in single-cylinder research engines with large windows has proven to be very useful for this purpose. However, experiments in such “optical” engines have two major drawbacks. First, optical engines are often significantly modified from the production engine, cannot operate over the full load-speed range, and are resource-intensive facilities. Second, like every experiment, also optical measurements can only access a small subset of the physically relevant quantities. Already the simultaneous acquisition of two quantities is challenging. To address the first issue, imaging through endoscopes [1, 2] or, even less invasive, point-like measurements via single-port probes have been employed. The second drawback applies much less to multidimensional simulations, which supply information on many quantities throughout the entire computational domain. However, - as in fact in the data evaluation of experiments - simplifying assumptions need to be made, potentially reducing the accuracy of the results. Since all these techniques for examining air/fuel mixing (and other in-cylinder phenomena) have their unique drawbacks, but also complement each other, the current work applied them together in the same optical engine.

Laser-induced fluorescence (LIF) of a “tracer” added in small amounts to a non-fluorescing surrogate fuel has become the tool of choice to image mass and heat-transfer phenomena in IC engines [3]. Most work pertains to liquid fuels with excitation by a pulsed UV laser where it is relatively straightforward to obtain sufficient LIF signal for qualitative visualization of the fuel. Image quantification is much more challenging, because fluorescence depends on pressure, temperature, and bath gas composition. In general, only pressure is known in the cylinder. However, under certain conditions, the LIF signal is proportional to the local ratio of the concentrations of tracer and oxygen. Thus, the (calibrated) signal can be directly interpreted as the local fuel/air ratio (FAR), which often is exactly the quantity of interest. This “FARLIF” approach, discussed in more detail in a section below, was first proposed by Reboux et al. [4] and has been applied in different variations by others since [5, 6, 7]. However, depending on the tracer, FARLIF can become inaccurate for high temperatures and residual gas fractions [8], and even when applicable, temperature still influences the result. Temperature can also be measured by LIF, in particular by exploiting a change of the excitation or emission spectrum via two-color measurements [9, 10, 11, 12, 13]. However, the low sensitivity of these two-color ratiometric methods negatively impacts precision.

Less frequently, tracer LIF has been used with gaseous fuels in optical engines. A general challenge is that almost all fluorescent tracers are liquid at room temperature. Thus, at

the elevated pressures upstream of the gas injector, only very low concentrations can be evaporated into the gaseous fuel, severely limiting the LIF signal strength. Nevertheless, qualitative visualizations of the fuel distribution in a methane-fueled engine were performed by Medaerts et al. [14] and Rubas et al. [15]. Quantitative LIF imaging of the fuel concentration in a motored hydrogen-fueled engine is documented in [16, 17, 18]. At 100 bar fuel pressure, the concentration of the highly volatile tracer acetone was only 0.25 vol%. These measurements were also compared to CFD simulations, showing that fuel dispersion was underpredicted by the simulation. Kirchweger et al. [19] used triethylamine (TEA) fluorescence to quantitatively determine the equivalence ratio via the FARLIF approach. However, local temperature differences between the measurement and the reference field could not be accounted for. More recently, Friedrich et al. analyzed the mixture formation in a CNG-DI engine by simultaneous imaging of TEA fluorescence and IR absorption [20] as well as TEA fluorescence and particle image velocimetry [21]. They showed the efficacy of TEA for quantifying the equivalence ratio. Local variations in temperature were not accounted for, and IR absorption was used for qualitative visualization of the methane distribution.

The objective of the LIF imaging in this work is to provide quantitative two-dimensional measurements of the air/fuel (or fuel/air) ratio in a fired, methane-fueled engine. The two major challenges are the low signal level and the influence of the local temperature on the signal. The former is addressed by selection of anisole as a tracer, which is novel for gaseous fuels. The local temperature is determined utilizing two-color thermometry and this information is used to correct the FARLIF-based measurement of the local equivalence ratio.

In the past, various optical probes based on infrared (IR) absorption have been used to determine fuel concentration, residual gas concentration, and temperature inside the cylinder of SI engines [22, 23, 24, 25]. In the case of CNG-fueled engines accurate quantification can be difficult due to pressure and temperature changes over the cycle. The IR spectrum of methane, the main component of CNG, consists of distinct spectral lines that are affected by pressure broadening and the temperature-dependent distribution of rotational states. Thus, narrowband detection methods are very sensitive to environmental influences. The measurement system we use in this work is based on non-dispersive infrared (NDIR) absorption spectroscopy. This method has been applied in gasoline engines using empirical models and requiring in situ calibration [23, 26]. Because of the structural simplicity of the methane molecule, quantification of NDIR absorption spectroscopy based on physical rather than empirical approaches is possible [27, 28]. The method deployed here is based on dual-band detection and modeling of the  $\nu_3$  anti-symmetric C-H stretch absorption band of methane ( $\text{CH}_4$ ) located around 3.3  $\mu\text{m}$ , allowing the simultaneous determination of fuel concentration and gas temperature inside a small measurement volume in the vicinity of the spark plug.

For CFD simulations the prediction of mixing of two gas phases is challenging, especially in the context of industrial

applications with the demand for short simulation times. Recent studies showed acceptable simulation results compared to optical measurements of methane injection by application of the numerical high-resolution method large-eddy simulation (LES). But the RANS approach has the potential for useful results while enabling shorter “wall time” [29, 30, 31, 32, 33]. Thus, the experimental techniques developed in this work were compared to results from CFD simulating mixture formation in the engine at a moderate cost level with a commercial code.

In this article, we first discuss the engine experiment and the essential features of each experimental technique and the simulation. Typical results are then first discussed separately, but the main idea of the article is to compare simultaneous LIF imaging and IR absorption measurements. Additionally, the experiments are compared to the CFD simulation, which in particular gives insight into experimental artifacts associated with heat transfer and extends the spatial domain beyond what can be examined via the spark plug probe and imaging through the cylinder window.

## Experiment

### Engine

The experiments were performed in an optically accessible single-cylinder engine at Volkswagen’s corporate research center. Engine parameters and operating conditions are summarized in [Table 1](#). (The crank angle convention in this article assigns 0°CA to combustion top-dead center (TDC), i.e., crank angles during intake and compression are negative.) The crank-angle resolved pressure was measured in intake, exhaust, and cylinder at 90 kHz sampling frequency, while intake and exhaust temperatures were measured at 4 Hz.

**TABLE 1** Engine parameters and operating condition.

Engine	4 valves, pent-roof
Cylinders	1
Compression ratio	8
Displacement	374 cm <sup>3</sup>
Bore/stroke	74.5 mm/85.9 mm
Speed	1500 min <sup>-1</sup>
Fuel	CH <sub>4</sub> + 0.07 vol% anisole
Intake oxygen conc.	21% (air)
Intake pressure	780 mbar (absolute)
$\lambda$ global	1.0
IMEP	4.4 bar
Intake valve opens	-334°CA
Intake valve closes	-184°CA
Exhaust valve opens	167°CA
Exhaust valve closes	347°CA
Start of injection	290°CA
End of injection	-334°CA
Ignition timing	-10°CA

The custom engine head was typical for a four-valve spark-ignition engine, with the pent roof and the cylinder sleeve as well as the piston partly made from fused silica. This enabled optical access to the top 55 mm of the stroke and the pent-roof combustion chamber. A fused silica window (diameter 65 mm) in the flat piston top provided additional optical access via a Bowditch-type piston extension and a 45°-mirror. The IR absorption sensor with its integrated spark electrode was mounted in the centrally located M12 spark-plug bore.

The engine was fueled with methane of 99.995% purity (grade 4.5) seeded with anisole (methoxybenzene, C<sub>7</sub>H<sub>8</sub>O, boiling point 154°C) for LIF imaging. Experiments in a metal engine at full load and high boost had shown that the concentration of anisole used here did not lead to abnormal combustion like knocking or pre-ignition. The photophysical aspects of anisole as a tracer are discussed below. To mix the gaseous fuel with the normally liquid tracer, a high-performance liquid chromatography (HPLC) pump metered anisole into the nozzle of a carburetor-like evaporator upstream of a pressure vessel. This allowed keeping the anisole concentration constant for different fuel flows when operating the engine at different speeds. The methane flowing through the evaporator’s Venturi nozzle was slightly pre-heated to 30°C and its mass flow controlled to maintain a pressure of 7 bar in the vessel. The vapor pressure of anisole at 30°C is 6.8 mbar, corresponding to a volume fraction of 0.1% at 7 bar. To prevent condensation, the anisole flow was controlled to 0.07% by volume (0.5% by mass) in methane. For comparison, in previous engine experiments with liquid fuel, 2.5 vol% anisole in isoctane were used, the limitation being excessive laser absorption for higher concentrations [34, 35].

The fuel pressure was regulated down to 5 bar before the fuel was mixed with the mass-flow controlled intake air flow by one of two possible procedures. A controller calibrated for methane provided a well-known fuel mass flow that was continuously injected far upstream of the engine into a Venturi-type flow constriction. Mixing was further promoted by four static mixing elements downstream of this injection point. The air/fuel mixture is expected to enter the combustion chamber spatially and temporally homogeneous, and thus allows computing a “global” air/fuel ratio  $\lambda_{\text{global}}$ . The calculated  $\lambda_{\text{global}}$  was verified by an exhaust gas analyzer. This air/fuel-mixing procedure was used for calibration purposes. Alternatively, for the actual mixing measurements, a commercial CNG injector (Bosch NG 2) injected the fuel into the intake pipe close to the engine (see [Figure 9](#)). This is similar to current production engines, where port-fuel injection (PFI) is implemented. For the PFI measurements the exhaust gas analyzer determined the injection duration that yielded the desired mean  $\lambda_{\text{global}}$ . Several injection timings and air/fuel ratios were investigated, but since the results are similar as far as an assessment of the diagnostic techniques is concerned, this article reports on a single operating point at 1500 rpm with stoichiometric air/fuel ratio ( $\lambda_{\text{global}} = 1$ ) and an intake pressure of about 780 mbar. Ignition at -10°CA resulted in an indicated mean effective pressure (IMEP) of 4.4 bar with a

peak pressure of 21 bar. The engine was fired for about 50 cycles before starting the optical measurements, which were then also performed in continuously fired operation.

## Tracer-LIF Imaging

**Fuel-Air LIF** For weak excitation at a given wavelength and low tracer number density, the detected fluorescence signal  $S$  is given by the linear relation:

$$S = I_{\text{laser}} V n_{\text{tr}}(p, T) \sigma_{\text{abs}}(T) \phi_{\text{fl}}(T, p, n_i) \Omega \eta, \quad \text{Eq. (1)}$$

where  $I_{\text{laser}}$  is the incident laser intensity,  $V$  the probe volume,  $n_{\text{tr}}$  the tracer number density,  $\sigma_{\text{abs}}$  the absorption cross-section,  $\phi_{\text{fl}}$  the fluorescence quantum yield (FQY), and  $\Omega$  as well as  $\eta$  are the collection and quantum efficiencies of the detection system, respectively. Apart from the desired quantity  $n_{\text{tr}}$  (proportional to the fuel number density), also the pressure  $p$ , the temperature  $T$ , and the number density of all bath-gas species  $n_i$  potentially influence the LIF signal. In the engine, only the pressure can be measured easily, while local temperature and composition are unknown, the former primarily because in fired operation residual gas mixes with the fresh charge.

For most aromatic fluorophores, the important bath-gas species is oxygen. Quenching by oxygen significantly reduces the FQY of aromatic fluorophores by non-radiative collisional depopulation processes [8, 36, 37]. Considering oxygen quenching, the FQY is given by:

$$\phi_{\text{fl}} = \frac{k_{\text{fl}}}{k_{\text{tot}} + \tilde{k}_{\text{q}}^{\text{O}_2} n_{\text{O}_2}}, \quad \text{Eq. (2)}$$

where  $k_{\text{fl}}$  is the rate of spontaneous emission,  $\tilde{k}_{\text{q}}^{\text{O}_2}$  the rate coefficient of quenching by oxygen with oxygen number density  $n_{\text{O}_2}$ , and  $k_{\text{tot}}$  the rate of all other deexcitation mechanisms. All these terms are temperature-dependent. If quenching by oxygen is the dominant deexcitation process,  $\tilde{k}_{\text{q}}^{\text{O}_2} n_{\text{O}_2}$  considerably exceeds  $k_{\text{tot}}$  such that  $k_{\text{tot}}$  can be neglected in the denominator. Substituting this approximated FQY into Equation 1, the measured LIF signal  $S$  becomes directly proportional to the equivalence ratio  $\phi$ , or inversely proportional to the relative air/fuel ratio  $\lambda$  (Note the ambiguity of  $\phi$  and  $\lambda$  with their meaning in spectroscopy, for example with  $\phi_{\text{fl}}$  in Equation 1. Both are the symbols traditionally used in this context.):

$$S \sim \frac{n_{\text{tr}}}{n_{\text{O}_2}} \sim \lambda^{-1} = \phi. \quad \text{Eq. (3)}$$

This FARLIF approach, originally due to Rebox et al. [4], enables measuring  $\lambda$  without knowing the local gas composition, even if fresh charge is mixed with residual gas from the previous cycles. However, since  $\sigma_{\text{abs}}$  as well as  $\phi_{\text{fl}}$

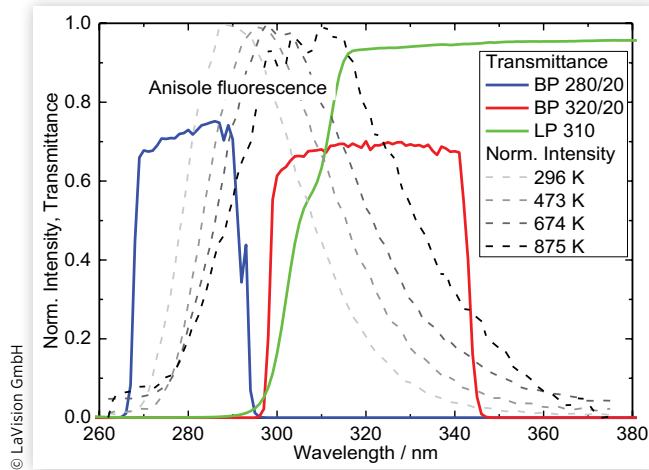
depend on ambient conditions like temperature or pressure, these variables have either to be measured, too, or appropriately be considered in calibration. E.g., pressure influences are minimized by recording measurements and corresponding calibration images at the same crank angle, although Scholz et al. [38] showed that FARLIF of toluene is almost pressure independent for absolute pressures larger than 500 mbar. However, temperature is not irrelevant, as discussed later.

In this work, anisole is used as a fluorescent tracer. Its photophysical properties at elevated temperatures and pressures are documented in [36, 39, 40]. A recent theoretical and experimental comparison with toluene indicated the potential of anisole as a brightly fluorescing tracer [41], and first experiments in an endoscopically accessed engine confirmed that indeed much higher signal than with toluene was possible [2, 35]. Tran et al. [36] showed for anisole excited at 266 nm that the fluorescence is inversely proportional to  $n_{\text{O}_2}$  for a temperature range of 473 K to 573 K at elevated pressure. To verify the validity of Equation 3 for our experimental conditions, we varied  $\lambda$  by successively substituting air with pure nitrogen, while keeping the fuel content constant. Image series at different crank angles, and thus different temperature-pressure combinations were acquired. We found that the LIF signal linearly depends on  $\lambda^{-1}$  for the interval  $0.2 \leq \lambda \leq 1$ . Values greater than 1 were not covered, because for these conditions the oxygen content is high anyway. The maximum deviation of  $\lambda$  from linearity occurs at  $\lambda = 0.2$ , where the relative oxygen content, and thus  $\tilde{k}_{\text{q}}^{\text{O}_2} n_{\text{O}_2}$ , is smaller compared to the rest of the interval. Thus, only in presence of large fractions of residual gas, for example just after the intake valve opens, FARLIF may yield inaccurate results, but for most conditions Equation 3 is a good approximation here.

Figure 1 shows anisole fluorescence spectra after 266-nm excitation for different temperatures at 1 bar absolute pressure. Each spectrum is normalized to its maximum intensity. The peak of the fluorescence spectrum shifts about 20 nm to longer wavelengths from 296 K to 875 K. As with other aromatic tracers [41], this red-shift can be exploited by detecting the fluorescence in two separate spectral windows (“colors”) and then relating the ratio of these two measurements to temperature. Figure 1 additionally shows the transmission characteristics of the dichroic beam splitter and the two bandpass filters that were used in our work for this purpose. After suitable calibration, the temperature information then can be used to account for the temperature dependencies discussed above.

**Optics and Data Acquisition** A schematic drawing of the imaging system is shown in Figure 2. The beam from a frequency-quadrupled Nd:YAG laser at 266 nm was guided through an energy monitor reflecting 8% of the laser light onto a detector to measure shot-to-shot fluctuations. The relative shot-to-shot energy fluctuations measured by this device typically were 6% (one standard deviation). A combination of cylindrical and spherical lenses then formed a sheet that was reflected 90° upwards by the mirror in the Bowditch-piston assembly. After passing the fused silica piston window, the sheet had a thickness of about 1 mm and was placed in

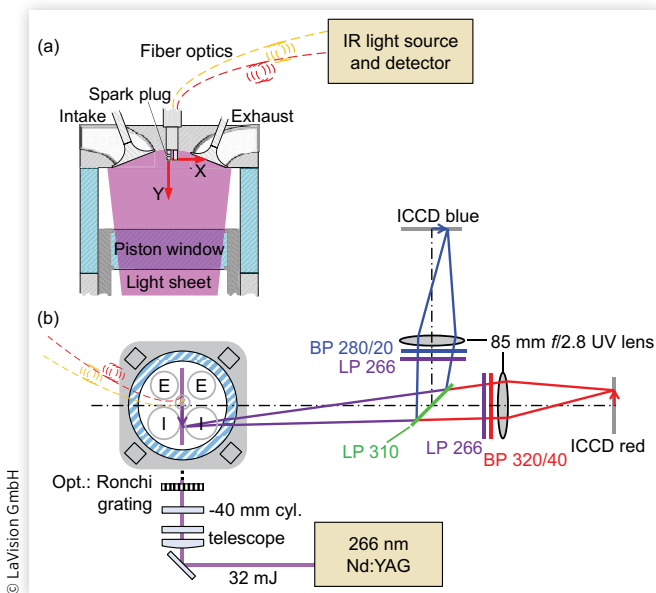
**FIGURE 1** Normalized anisole fluorescence spectra after 266-nm excitation for different temperatures at 1 bar measured by Faust et al. [39]. Additionally, the transmittances of the filters and beam splitters used here are plotted.



the central symmetry plane of the combustion chamber as shown in Figure 2b. The average laser shot energy in the observation area was 27 mJ. Because the piston window is only 65 mm in diameter, some of the 74.5-mm bore cannot be illuminated, as indicated in Figure 2b. Also, the flat-top piston is in the field of view after  $-90^\circ\text{CA}$ .

For some experiments, a reflective-transmissive Ronchi grating was placed between the sheet-forming optics and the Bowditch-piston mirror, creating a periodic, lateral intensity modulation in the light sheet. With Fourier-space post-processing, this modulation can be utilized to reject fluorescent

**FIGURE 2** Arrangement of optics and engine cylinder for LIF imaging and IR absorption measurement. (a) Side view of the combustion chamber, (b) top view of cylinder and optics.



out-of-plane background at the expense of spatial resolution. In the current work, this technique, usually termed “structured laser illumination planar imaging” (SLIPI) [42, 43, 44, 45], was only used for the temperature calibration in the standing engine, described below.

Following the two-color strategy for measuring the temperature in addition to the FAR, the anisole fluorescence is spectrally separated into a “blue” and a “red” part by means of a 310 nm dichroic beam splitter (see also LP 310 in Figure 1). A 266 nm longpass edge filter in front of each camera lens suppresses remnants of laser light. In addition, bandpass filters at  $280\text{ nm} \pm 10\text{ nm}$  and  $320\text{ nm} \pm 20\text{ nm}$  further narrow the “blue” and “red” spectral range of detection, respectively. Two intensified CCD cameras (LaVision intensified relay optics (IRO) and Imager E-lite CCD) with UV camera lenses (LaVision,  $f = 85\text{ mm}$ ,  $f/2.8$ ) image the field of view at a projected pixel size of 0.07 mm/pixel.

PFI measurement and calibration are performed in two consecutive steps: First, the engine is operated in fired PFI mode to image mixture formation under realistic engine conditions. Second, the engine is motored and supplied with a homogenous air/fuel mixture serving as quantitative calibration as well as a correction for inhomogeneity in illumination and detection in the PFI measurements of step one. The calibration images are called “flatfield” images in the following. These images are captured in motored operation in order to prevent inhomogeneities caused by residual burnt gas from previous cycles.

Phase-locked (at a repetition rate of 12.5 Hz) to a particular crank-angle, images of 20 consecutive cycles for PFI and for flatfields are taken, respectively. In order to prevent damage to the optical engine caused by high temperatures in fired mode, PFI data are recorded in sets of 6 crank angles each, with sufficient time in motored operation in between to cool down the engine. Flatfield images are recorded during this motored operation, also in sets of 6 crank angles each. In total, 49 crank angles from  $-360^\circ\text{CA}$  to TDC were recorded. At the very end, background images (motored operation without fuel injection) over the full crank angle range are recorded.

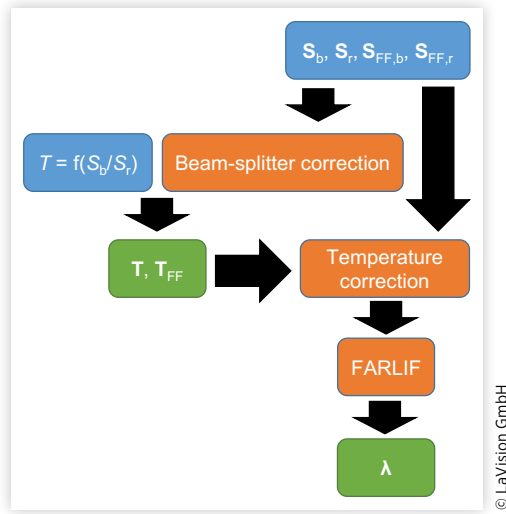
**Image Quantification** This section outlines the basic concept of image quantification in this work. Details are provided in subsequent sections. Figure 3 shows a schematic of the LIF data processing.

According to Equation 3, the relative air/fuel-ratio  $\lambda$  is inversely proportional to the LIF signal. The measured PFI images  $S$  are corrected for inhomogeneities in illumination and detection by dividing them by flatfield images  $S_{\text{FF}}$  taken at the same crank angle, and then calibrated by the global air/fuel ratio  $\lambda_{\text{global}}$  that was set during the flatfield acquisition. This yields the local  $\lambda$  of the PFI measurements:

$$\lambda = \left( \frac{S}{S_{\text{FF}}} \right)^{-1} \lambda_{\text{global}} \quad \text{Eq. (4)}$$

However, the fluorescence signal depends on temperature, and the flatfield images were taken in motored operation,

**FIGURE 3** Schematic overview of the data processing for LIF imaging.



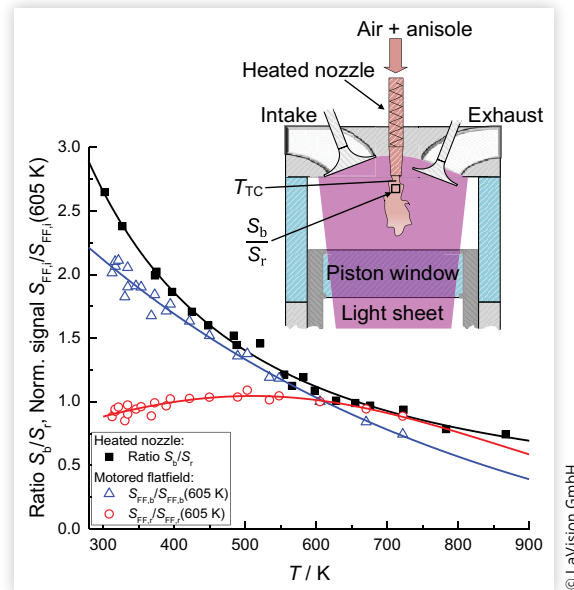
where the in-cylinder temperature level before ignition is on the order of 100 K lower than in fired operation (see Figure 5b). Additionally, there is local temperature inhomogeneity. Hence, all images need to be corrected for temperature. This is done based on temperature correction functions, which have to be determined first. Finally,  $\lambda$  is computed by Equation 4 using one of the temperature-corrected images of the two cameras.

In detail, inputs of the processing are the PFI LIF signals  $S_b$ ,  $S_r$  and the flatfield images  $S_{FF,b}$ ,  $S_{FF,r}$  where “b” and “r” label the signals in the “blue” and “red” channel, respectively. In a first step, all images are binned  $10 \times 10$  pixels corresponding to a spatial resolution of 0.7 mm. After this, the images are corrected for background and shot-to-shot laser energy fluctuations. Then, a beam-splitter correction is applied to all images used for the determination of the local temperature  $T$ . This temperature information is used to correct the temperature-caused signal differences in flatfields  $S_{FF,i}$  and PFI measurements  $S_r$ . After these steps, FARLIF is used to compute the temperature-corrected local relative air/fuel ratio  $\lambda$  for the PFI measurements.

**Temperature Calibration** Temperature calibration is done in situ in the standing engine similarly to [2]. The spark plug is removed and a heated fused silica nozzle is fitted into the bore as shown in the inset of Figure 4. For safety, the methane flow was replaced by air for this calibration. Hence, a mixture of pure air and anisole continuously flows through the heated nozzle, enters the combustion chamber and exits through an opened exhaust valve. The gas temperature  $T_{TC}$  was measured by a thermocouple where the mixture exits the nozzle in the field of view of the cameras.  $T_{TC}$  was varied between 300 K and 870 K with 100 images averaged for each temperature.

Since in particular these heated-nozzle images were found to suffer from out-of-plane fluorescence, the Ronchi grating,

**FIGURE 4** Parametrization of the relationship between LIF signal ratio and temperature based on a heated nozzle flow. The inset shows the principle of the in-situ calibration with the heated nozzle. In addition, for both channels the temperature dependence of the LIF signals, determined from motored engine operation and normalized to the signal at 605 K, is plotted.

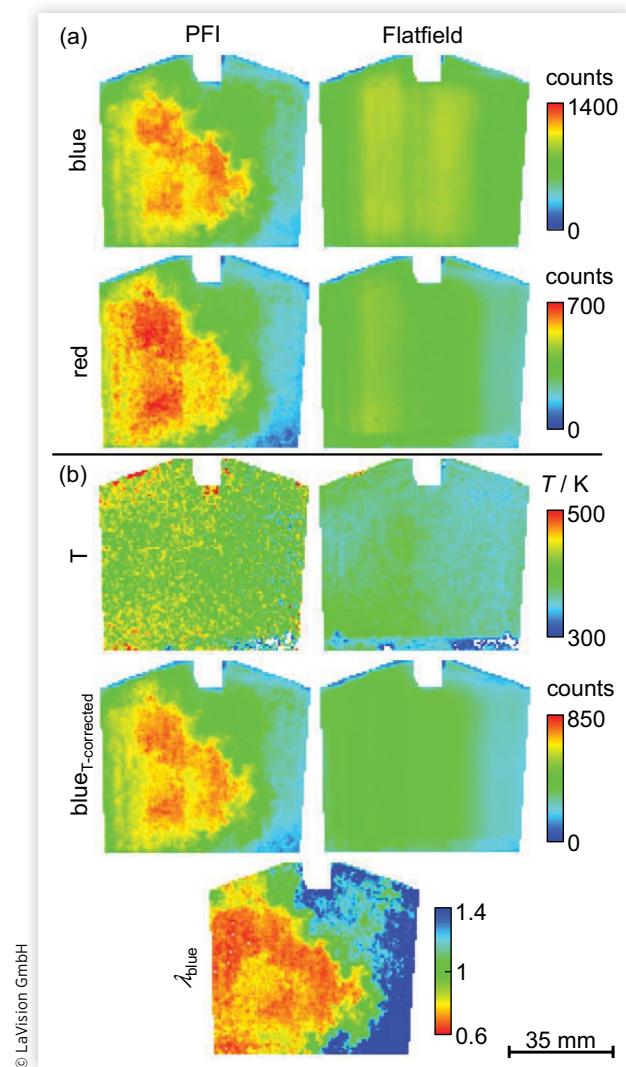


indicated in Figure 2, was placed in the laser path, and SLIPI procedures were used to correct all images for background. The dependence of the channel ratio  $S_b/S_r$ , averaged over the region indicated in the inset of Figure 4, on  $T_{TC}$  was measured (see diagram in Figure 4). The data were phenomenologically parametrized by a three-parameter exponential function, allowing pixel-wise computation of the local temperature from the signal ratio.

**Beam Splitter Correction** The angular dependence of the dichroic beam splitter affects the relative assignment of the fluorescence signal to a specific channel significantly. Even in case of uniform temperature and illumination, a variation in signal ratio will occur over the whole field of view, since every pixel receives light at slightly different angles with respect to the beam splitter. In fact, the example raw images in Figure 5a show that both the PFI and flatfield images differ between red and blue channel, with a systematic horizontal shift in intensity. A correction for such beam-splitter effects was already implemented in [12]. We extended that procedure by considering also the temperature information in the correction functions, since the temperature influences the magnitude of the angular dependence through the red-shift of the anisole fluorescence spectrum.

**Temperature Correction** After beam-splitter correction of the color-ratio images, the field-wide temperature is determined. Using this temperature, PFI and flatfield images are

**FIGURE 5** Demonstration of the temperature correction for a single shot at  $-160^{\circ}\text{C}$ . (a) Shows the uncorrected flatfield and PFI images for the blue and the red channel. (b) Shows the calculated temperature as well as the temperature-corrected image in the blue channel and the deduced (temperature corrected) air/fuel-ratio.



corrected to signal values that would be expected if the images had been recorded at uniform and equal temperature. In Figure 4, the temperature dependence of the LIF signals, normalized to the signal at 605 K (arbitrarily chosen) is plotted for both channels. The tracer concentration in the mixture flowing through the heated nozzle fluctuated, since the tracer metering system was inaccurate at the low flow rates used then. This did not affect the signal ratio, but the absolute signals needed to determine the temperature correction functions. Thus, for his latter purpose flatfields from the motored engine are used. The absolute signals originate from averaging the flatfield signal for both channels separately over the area indicated in the inset of Figure 4. The temperature is determined based on the ratio method applied to the flatfields in that very region.

For the example PFI and flatfield image pairs shown in Figure 5a, the resulting temperature images are shown in the top row of Figure 5b. Although there is a - presumably real - horizontal temperature gradient across the field of view, this is much less than what would have been expected from the blue/red image pairs in Figure 5a, meaning that much of that visually obvious difference was due to the beam splitter. Figure 5b also shows that the average temperature in the motored flatfield is significantly lower than with continuously fired PFI. The temperature correction accounts for both the spatial temperature variation within the flatfield and the overall underestimation with respect to fired conditions.

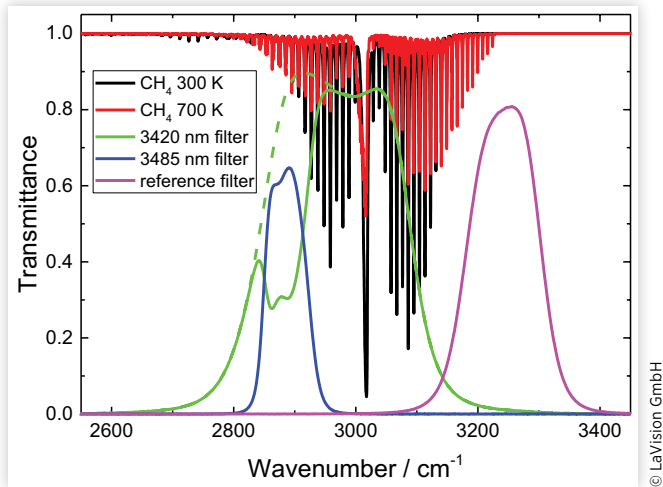
After temperature correction, the corresponding  $\lambda$  images can be determined based on either of the two channels. While the variation in signal ratio caused by the beam splitter impacts the temperature determination, and thus has to be corrected in this case, in the FARLIF-quantification of  $\lambda$  according to Equation 4, this influence is already eliminated by the flatfield correction.

**Single-Shot Precision** In all flatfields,  $\lambda$  is spatially homogeneous and stoichiometric. Hence, the scatter of  $\lambda$  around unity in the temperature corrected flatfields reflects the precision of the measurements at  $\lambda = 1$ . The standard deviation of one binned pixel (an area of  $0.7 \times 0.7 \text{ mm}^2$ ) over 20 consecutive single shots was  $\sigma(\lambda) = 0.05$ .

## IR Absorption Sensor

The IR absorption-based sensor and initial validation in a near-production engine are described in detail in [27, 28]. Briefly, the measurement system is a modification of the internal combustion optical sensor (ICOS) from LaVision GmbH. It consists of a broadband light source (150 W quartz-tungsten-halogen lamp), a modified spark-plug probe, and a detection unit. The modified spark plug is equipped with a small metal cage with a 0.96 cm long absorption path next to the spark electrodes. The light of the lamp is modulated with a frequency of 30 kHz, allowing correction of the signal for background radiation. The detection unit is a cascade of several bandpass filters in front of infrared detectors for the detection of multiple molecular species. Here, three filters are used for the quantification of the fuel concentration, which are shown in Figure 6 along with spectra of the methane  $\nu_3$  absorption band for 300 K and 700 K. Two of the filters, located around  $2920 \text{ cm}^{-1}$  (3420 nm filter) and  $2870 \text{ cm}^{-1}$  (3485 nm filter), allow detection of methane density and temperature inside the measurement volume based on the absorption of the  $\nu_3$  band. Another filter, located around  $3090 \text{ cm}^{-1}$  (3240 nm, reference filter), serves as an offline-reference for signal correction but is also influenced by absorption of methane. This influence is taken into account in the data analysis process. We note that it is difficult to eliminate the fuel absorption in the reference channel, since a spectral shift towards higher frequencies would lead to increasing overlap with water absorption bands centered around  $3700 \text{ cm}^{-1}$ .  $\text{ZrF}_4$  fibers guide the light from the lamp to the

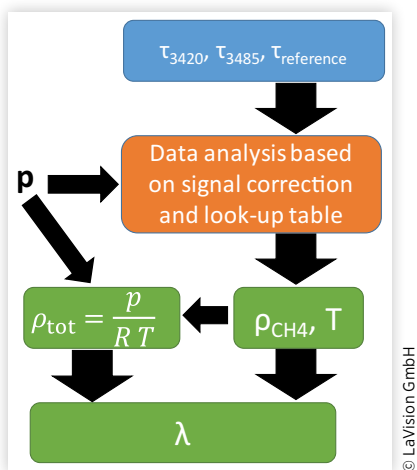
**FIGURE 6** Methane transmission spectra for 300 K and 700 K at 10 bar, 2% CH<sub>4</sub> mole fraction, and 0.96 cm long absorption path calculated using the HITRAN database and transmittance curves for the three filters in the IR absorption sensor. Parts of the 3420 nm band (dashed green) are influenced by the 3485 nm filter, resulting in an effective filter transmittance that is shown in solid green.



probe and back to the detection system, whereas sapphire fibers are used inside the probe. The latter limit the detection to frequencies  $>2600 \text{ cm}^{-1}$ . The measured light intensity with its sampling rate of 30 kHz is mapped onto the engine's crank angle trigger by the detection unit.

Figure 7 shows a schematic overview of the data analysis process. First, we calculate transmittance values from the measured voltage output of the detectors using parts of the cycle in which methane is not present as described in ref. [28]. We use a correlation algorithm to determine methane density and temperature from the two filter signals using a look-up table and the measured pressure provided by the engine

**FIGURE 7** Schematic overview of the data analysis for the IR absorption sensor measurements.



instrumentation [27, 28]. The look-up table links pressure, temperature, density, and transmittance through Beer-Lambert's Law and is calculated from the HITRAN database [46]. We use these first estimates for density and temperature to determine the amount of fuel absorption in the reference filter. This procedure leads to a correction signal that is not related to any absorption but caused by opto-mechanical influences on the sensor probe during the engine cycle (e.g. beam steering). The correction signal is applied to the measured transmittances of the 3420 nm and 3485 nm filter. The signal correction is repeated several times until convergence (typically after 3 to 5 iterations) to final values for the transmittances occurs. These final transmittances result in final values for methane density and temperature via the look-up table discussed above, and we use the temperature to calculate the total gas density via the ideal gas law. Finally,  $\lambda$  is calculated from the methane density  $\rho_{\text{CH}_4}$  and the total gas density  $\rho_{\text{tot}}$  with a stoichiometric factor of 9.52 as

$$\lambda = \frac{\rho_{\text{tot}} - \rho_{\text{CH}_4}}{9.52 \cdot \rho_{\text{CH}_4}} \quad \text{Eq. (5)}$$

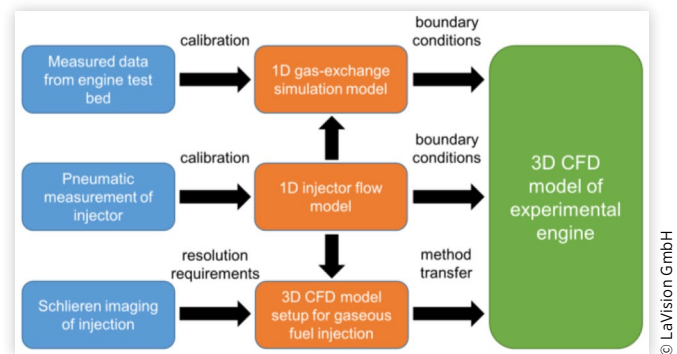
Note that we do not measure the residual gas concentration, which was considered to be fairly low at the engines operating point we employ here. Thus, we neglect the residual gas concentration, assuming that the total gas density is equal to the density of air. This causes the calculated  $\lambda$  to be an upper limit.

## CFD Simulation

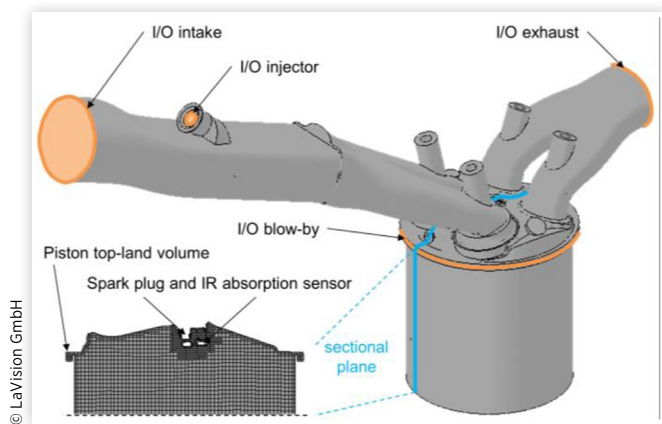
The commercial CFD software VECTIS version 2017.1 was used to perform engine simulations close to the experimental conditions. The Reynolds-averaged Navier-Stokes (RANS) approach with the two-equation  $k-\epsilon$  turbulence model in a finite volume discretization scheme was applied. This is a state-of-the-art method for engine development in an OEM environment. Details on the numerical approach can be found in [47].

Figure 8 schematically shows the overall workflow to create a suitable CFD model. The spatial discretization of the computational domain and in particular the inlet and outlet

**FIGURE 8** Workflow of the CFD model development.



**FIGURE 9** Geometry of computational domain with inlet and outlet boundaries (I/O) marked in orange color. The inset on the bottom-left shows the central cut plane that will be used to visualize the results.



(I/O) boundary conditions were chosen based on extensive previous characterization of the flow through the engine and the injector. A complete description of these auxiliary measurements is beyond the scope of this article, but a brief summary is given below.

**Simulation Domain** Figure 9 shows the geometry of the computational domain with intake pipe, port fuel-injector seat, intake ports, combustion chamber, and exhaust ports. To preserve the geometric compression ratio of the optical engine and provide a boundary for modeling blow-by, a volume corresponding to the piston top-land is connected to the stationary boundary of the cylinder head gasket. Four engine cycles were simulated to evolve quasi-steady operating conditions. Results are taken from the fourth cycle.

For spatial discretization, a base mesh size of 2.5 mm was chosen. The combustion chamber was represented with 1.25 mm numerical mesh discretization, with a resolution of 0.75 mm at the spark plug and 0.375 mm near intake valve seat. Near the injector nozzle the mesh resolution is finer than 0.2 mm. Preliminary studies including Schlieren imaging in a pressure chamber had been carried out to determine the requirements for the geometric discretization of the PFI nozzle area. Overall, the CFD domain contains less than  $10^6$  cells at bottom-dead-center. A time step of  $0.01^\circ\text{CA}$  was used, with  $0.005^\circ\text{CA}$  during fuel injection in order to comply with the Courant condition. Parallelization into 32 partitions allowed computing four cycles in ten days wall time.

**Boundary Conditions and Combustion Model** The conditions at the I/O boundaries, indicated in orange color in Figure 9, were set based on a one-dimensional (1D) gas-exchange model of the engine representing the complete flow system in the test cell. This 1D model was “calibrated” to yield the measured crank-angle resolved pressure traces in the cylinder, intake, and exhaust. At the intake and exhaust I/O boundaries of the 3D CFD, pressure and temperature from

the 1D model were then prescribed as a function of crank angle. Since the optical engine had been found to have considerable blow-by through the piston rings, an additional I/O boundary was defined at the stationary representation of the piston top-land volume. Its mass flow rate as a function of crank angle was also determined from the 1D gas-exchange model. The gaseous fuel injection was also prescribed as mass flow rate vs. crank angle. A dedicated 1D flow model of the injector was used to calculate the time-resolved mass flow rate during injection for the relevant pressure ratio. Parameters in this 1D model were set based on pneumatic measurements in a pressure vessel.

The constant-temperature wall boundary conditions were obtained from the 1D gas-exchange model. For this purpose, the CFD domain was structured into regions with similar wall temperatures, e.g. intake pipe, intake ports, intake valves, cylinder head, cylinder wall, piston, exhaust valves, and exhaust ports. Wall temperatures of geometric details that are not resolved by the 1D gas-exchange model, such as spark plug and IR absorption sensor, were derived from adjacent boundaries. In particular, the temperature of the sensor was set to 450 K.

For the combustion modeling the *G*-equation model is used, which enables locating the position of the flame front [48]. A reduced power law equation is utilized for the flame propagation with a formulation by Metghalchi and Keck [49] for laminar flame speed. Details on the combustion modelling in VECTIS can be found in [50]. In the current work focusing on pre-combustion mixture formation, the accuracy of the combustion model is of lesser importance, but combustion as a whole is important because it strongly influences wall heat transfer.

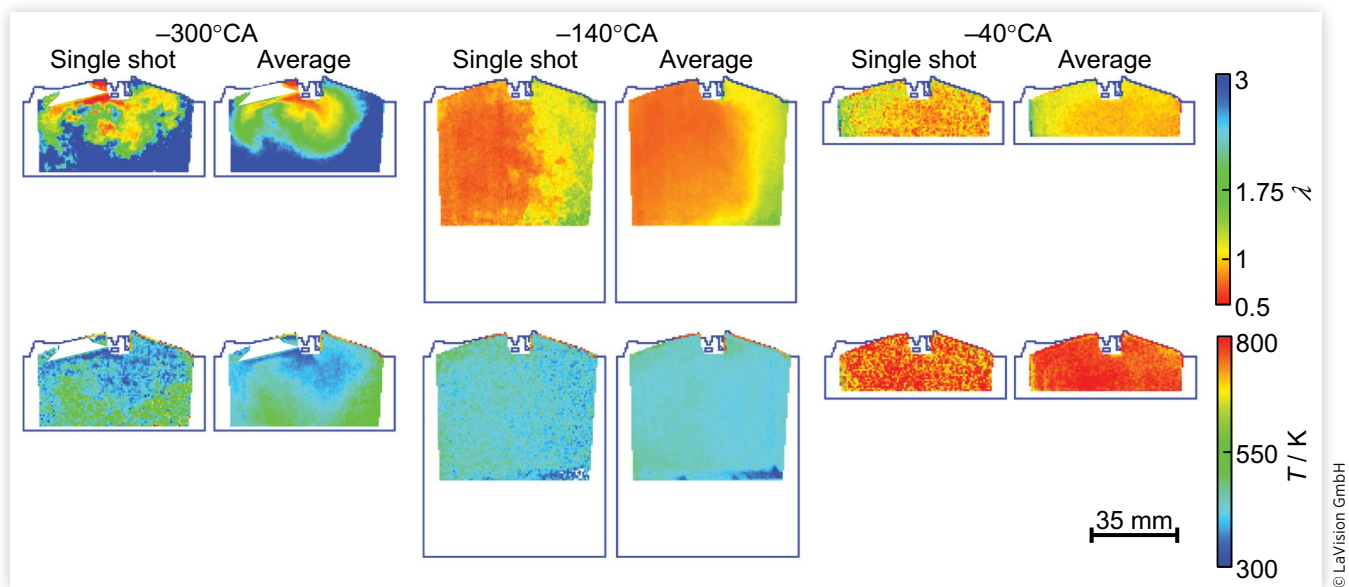
## Results and Discussion

### Tracer-LIF Imaging

Figure 10 shows examples of single-shot and ensemble-averaged images of  $\lambda$  and temperature during gas exchange ( $-300^\circ\text{CA}$ ), early compression ( $-140^\circ\text{CA}$ ), and close to ignition ( $-40^\circ\text{CA}$ ). At  $-300^\circ\text{CA}$  fuel-rich mixture enters the combustion chamber from the intake valves. In the single shot, small-scale structures due to turbulent mixing can clearly be seen. The boundary of the fresh charge gas appears sharper here than it really is because for clarity the color palette is clipped at  $\lambda = 3$ . However, beyond  $\lambda = 5$  the background signal dominates over the anisole LIF signal such that this value represents the upper detection limit at this crank angle.

The corresponding temperature images suffer from more noise, originating from the division of two noisy images, the limited sensitivity of the channel ratio to temperature, and pixel-level inaccuracies in the mapping of the two images. However, at  $-300^\circ\text{CA}$  temperature structures are still measurable, though with reduced resolution compared to  $\lambda$ . The inhomogeneity in temperature is consistent with that in  $\lambda$ , the incoming fresh charge being much colder than the surrounding gas.

**FIGURE 10** Single cycle and ensemble-average over 20 cycles of temperature-corrected air/fuel ratio and temperature distributions from LIF imaging for three selected crank angles. The boundary of the combustion chamber and intake valve is also shown.



At  $-140^\circ\text{CA}$ , in the single shots fine-scale structures from turbulent mixing are still visible in  $\lambda$ , but not in temperature anymore. Since the overall temperature level is still similar to that at  $-300^\circ\text{CA}$ , noise at a given  $\lambda$  is also similar. However, mixing has increased  $\lambda$  in the fuel-rich zone and thus decreased the LIF signal there as well as the contrast to the surrounding leaner gas. Both in  $\lambda$  and in temperature, horizontal stratification of the mixture is discernable, from rich and hotter on the left side to lean and cooler on the right. At first, it might be surprising that the presumably rich fresh charge is associated with higher temperatures, but as we will see later, due to the closed-valve PFI timing, the fresh charge is only rich for the earlier part of the intake stroke, followed by nearly pure air. The earlier, rich part of the charge encounters the hot residual gas, partially mixes with it, and becomes warmer than the lean remainder of the charge. Simultaneously, convection in tumble motion yields the spatial distributions that we measure. However, this level of detail would have been difficult to conclude from the LIF imaging alone, since the contrast in the temperature images is simply too low. Instead, it was from consulting also the CFD simulation, for example as shown in Figure 12, that we reconciled what first appeared to be measurement inaccuracy.

At  $-40^\circ\text{CA}$ , when temperatures are high, the LIF signal in the blue channel is much lower than in the early compression as shown in Figure 4, lowering the signal-to-noise ratio (SNR) in temperature and  $\lambda$ . The grainy small-scale structures visible in the single shots are due to noise, but the average  $\lambda$  field still shows large-scale inhomogeneity.  $\lambda$  ranges from values of about 1.2 at the very left end of the field of view to values slightly lower than 1.0 in most parts of the remaining area. Inhomogeneity in temperature is hard to distinguish from noise even in the 20-shot ensemble average. Overall, at

crank angles late in the compression, it may be advantageous to reduce resolution further in favor of noise reduction, since at least in  $\lambda$  small-scale structures are not expected anyway.

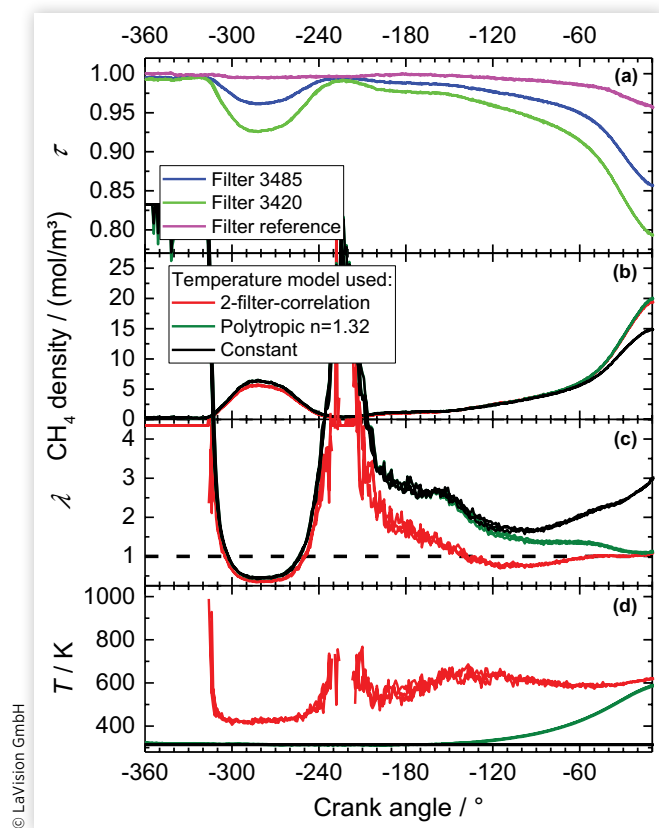
## IR Absorption Sensor

In contrast to LIF imaging, the IR absorption probe only allows for an integral measurement in a small detection volume, but at a high repetition rate. Figure 11 shows the measured transmittance data and the calculated density, the relative air/fuel ratio  $\lambda$ , and temperature, as well as the global value  $\lambda_{\text{global}} = 1.0$  set for the measurements. Panel (a) of Figure 11 shows the transmittance values for the three different detection channels defined by the corresponding filter transmission characteristics (see Figure 6). The other panels show the results using these transmittance values and the 2-filter-correlation described in Figure 7 and [28] (black). In addition, the panels show results using (1) an estimated temperature based on a polytropic compression (dark green) and (2) assuming a constant temperature (red). The polytropic temperature  $T$  is calculated from the measured pressure  $p$  with a starting temperature  $T_0$  equal to the engine coolant temperature (315 K) and a starting pressure  $p_0$  matched to the averaged measured values between  $-300^\circ\text{CA}$  and  $-260^\circ\text{CA}$  as:

$$T = T_0 \cdot \left( \frac{p}{p_0} \right)^{\frac{n-1}{n}}, \quad \text{Eq. (6)}$$

The polytropic coefficient of  $n = 1.32$  we employ here is based on long-term experience with CNG-fueled production engines and this optical engine at Volkswagen.

**FIGURE 11** Transmittance values and results of the IR absorption sensor measurements for injection of methane using the 2-filter-correlation, a polytropic temperature estimate, and a constant temperature. Each measurement is averaged over 100 cycles and repeated three times. The dashed black line in the  $\lambda$  panel shows the globally set value.



Looking at the results of the 2-filter correlation,  $\lambda$  (panel c) at the beginning of the cycle is above 4 (less than 2.6% methane), which is close to the detection limit of the system. After the intake valve opens at  $-334^\circ\text{CA}$ ,  $\lambda$  decreases, reaching  $\lambda \approx 0.35$  at  $-280^\circ\text{CA}$ , increases again to  $\lambda > 4$ , before it finally decreases. During the compression stroke from  $-180^\circ\text{CA}$  to  $0^\circ\text{CA}$ ,  $\lambda$  exhibits small oscillations and approaches the globally set value before ignition. Just before ignition at  $-10^\circ\text{CA}$ ,  $\lambda$  increases slightly to  $\lambda \approx 1.07$ . Overall, this is the typical behavior of an IC engine with closed-valve PFI. The injection ends with the opening of the intake valve, causing a methane “plug” upstream of the valves. Upon intake valve opening, this fuel enters the combustion chamber, passing the spark plug. The fuel is followed by almost pure air from the intake pipe, causing the sudden rise of  $\lambda$ . After intake valve closing, the tumble motion and turbulent mixing homogenize the mixture, until finally at the end of compression,  $\lambda$  at the spark plug is close to the globally set value.

Panel (d) of Figure 11 shows the measured temperature inside the measurement volume of the spark-plug probe. At the beginning of the cycle, the temperature is very high due

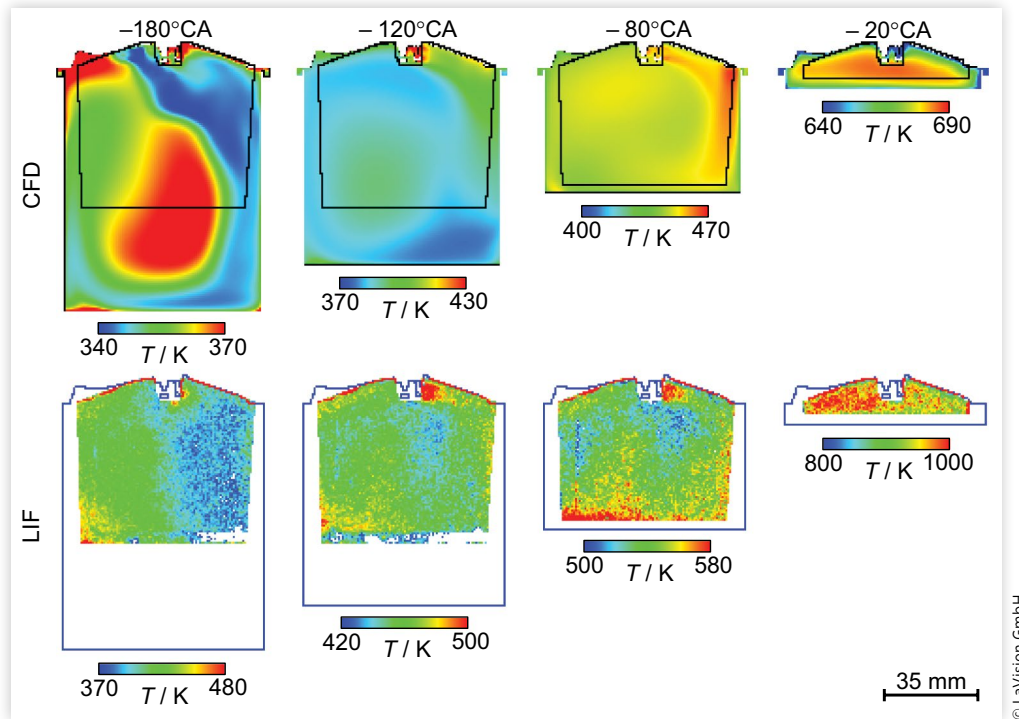
to residual burnt gas from the previous cycle. After opening of the intake valve, the temperature decreases to about 425 K at  $-300^\circ\text{CA}$  due to mixing of residual gas with fresh charge. This is much higher than the temperature of fresh charge (300 K) and the engine itself (315 K). This difference in temperature is likely caused by the metal cage of the spark plug probe that heats up during continuous firing and stays hot. The temperature rises again, cannot be determined around  $-220^\circ\text{CA}$  due to the very low methane density, and reaches a plateau after the beginning of the compression stroke.

This behavior is very different from the expectation from polytropic compression, shown as green lines in Figure 11b-d. Comparing measured and polytropic temperature, the measured temperature is always higher. The measured temperature represents a local value of the gas inside the metal cage of the spark plug, whereas the polytropic temperature can be understood as a mean value over the whole cylinder based on the pressure. The deviations can be assigned to the effects of heat transfer between the metal cage and the gas flowing through. Therefore, it is interesting to investigate how an inaccurate temperature model influences the determination of the primary measure, i.e.,  $\lambda$ .

For this reason, we also analyzed the experimental data either assuming a constant temperature (black curves in Figure 11) or the temperature predicted by a polytropic model (dark green curves in Figure 11). Note that using either of the three temperatures, the resulting density differs only slightly before about  $-60^\circ\text{CA}$ . Starting from this crank angle, the increase in density is less for a constant temperature than for a polytropic temperature or the measured temperature from the 2-filter-correlation. This is likely due to the increasing difference in temperature starting from about  $-120^\circ\text{CA}$ , which is shown in Figure 11d. The clearly incorrect assumption of constant temperature ultimately leads to  $\lambda \approx 3$  at ignition, which is unrealistically high. Although it is not surprising that the incorrect model of a constant temperature fails, it is still worth noting since in previous applications [51] for FAR determination in gasoline engines the effect of temperature on the photophysics of the fuel was neglected. The gross simplification works in that case because for liquid fuels, which consist of larger hydrocarbons, FAR quantification is possible by simple in-situ calibration of the measured signal as a function of the global FAR [51]. The reason is that the temperature and pressure dependencies of the 3.4- $\mu\text{m}$  absorption band are weak and, integrated across the whole band, their effects on the measured FAR cancels. In case of methane, the  $\nu_3$  band probed here consists of distinct absorption lines. Therefore, an exact description of the molecule's spectroscopy is required for quantification, which also involves knowledge of temperature.

In contrast to the phenomenon described above, the methane densities (Figure 11b) resulting from the 2-filter-correlation and the temperature from the polytropic model remain similar until ignition. However, the behavior of  $\lambda$  (panel c) differs significantly during compression from about  $-200^\circ\text{CA}$  to  $-30^\circ\text{CA}$ . With rising temperature during compression, the differences in temperature and  $\lambda$  decrease, as the polytropic temperature approaches the measured one.

**FIGURE 12** Crank angle evolution of temperature during compression from CFD simulations and ensemble-averaged from LIF measurements.



Nevertheless, if the polytropic temperature were used instead of the measured one, the evolution of  $\lambda$  would be determined qualitatively incorrectly. With the former,  $\lambda$  monotonically decreases in the probe volume, while with the latter, it is seen to actually reach a minimum at  $-110^\circ\text{CA}$  and then increase towards TDC. Note that the calculated *methane* densities (Figure 11b) resulting from 2-filter-correlation and the polytropic temperature model overlay almost perfectly (max. error is about 13% ( $-300^\circ\text{CA}$  to  $-250^\circ\text{CA}$ ) and about 6% at ignition). In conclusion, the impact of temperature in the calculation of  $\lambda$  is largely through determination of the *total* gas density (from pressure and temperature).

The 2-filter-correlation method measures the temperature inside the local measurement volume, which is clearly affected by heat transfer from the mirror and the metal cage. Measuring the temperature, as opposed to estimating it from a pressure-based model, was seen to be necessary for the correct calculation of  $\lambda$ , as the measurement of the gas composition (methane density and total gas density) takes place at exactly this location. However, the probe is not suitable for measuring the average temperature in the combustion chamber. An alternative setup for the IR sensor is to work with line-of-sight probes located at two opposing position in the cylinder wall, measuring across the cylinder. With this arrangement, no parts protrude into the combustion chamber, thus avoiding heat transfer with the gas.

For further confirmation of the observed thermal interaction of the spark-plug probe with the surrounding gas, we extracted center-plane temperature fields from the CFD

simulations and LIF imaging, shown in Figure 12. Even if the LIF temperature images suffers from noise and the temperature appears to be overestimated, CFD and LIF agree qualitatively. They both show that temperature around the spark plug differs significantly from the temperature in the rest of the cylinder. Downstream of the spark plug it is higher during early compression, and in the vicinity of the spark plug it is lower close to ignition (in fact the CFD shows higher temperatures at  $-20^\circ\text{CA}$  than the polytropic compression model). This is the same behavior as measured with the IR absorption sensor (see Figure 11). Thus, a physically consistent picture emerges: The sensor cage heats up during combustion and expansion. While the intake valve is open, the cage is still hot, but because of the fast flow through it, the temperature of most of the gas volume in the cage is nevertheless close to the temperature of the incoming charge. When the charge motion slows down after intake valve closure, the still hot cage heats up the gas in it. The temperature of the gas in the probe volume is now significantly higher than that of the bulk gas. Finally, during late compression, this difference reverses as the bulk gas is compressed to temperatures above the cage temperature.

## Inter-Experiment Comparison

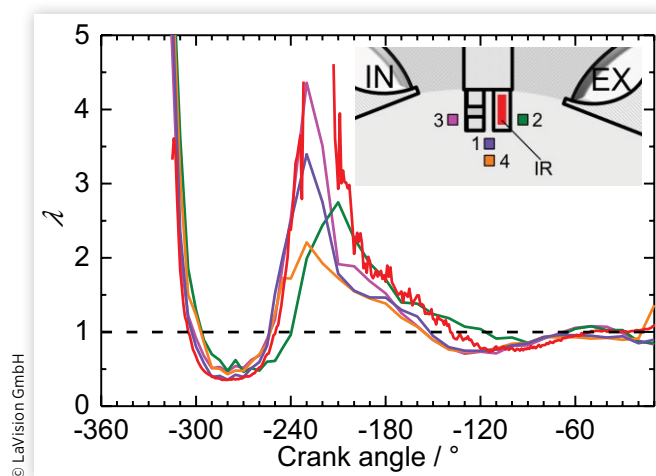
IR absorption measurements and LIF imaging were performed simultaneously. While the former determines the average  $\lambda$  over a short line in the optics cage next to the spark plug, the latter yields  $\lambda$  at almost any point in the field of view, but unfortunately not in the sensor cage. Therefore, the evolution

of  $\lambda$  determined by LIF imaging was examined in four different regions of interest (ROIs) located around the spark plug sensor and was compared to the results of the IR absorption measurement. The location of the ROIs and the resulting crank-angle series of  $\lambda$  are shown in Figure 13. ROIs 1, 2 and 3 are located close to the sensor to reflect the IR results, while ROI 4 was placed further away to check if background in the LIF images in the immediate vicinity of the reflective spark-plug sensor influenced the measurements. At  $2.1 \times 2.1 \text{ mm}^2$  each, the ROIs were chosen to fit approximately the projected area of the probe volume of the IR sensor.

As discussed above, closed-valve PFI causes charge stratification: First, very lean mixture enters the combustion chamber for a short time after the intake valves open at  $-334^\circ\text{CA}$ , followed by fuel-rich fresh charge, ending again with a lean mixture just before the intake valve closes, with homogenization during compression. In the early, lean phase and while the fuel-rich “plug” from PFI passes through the probe volumes, only small differences between all four ROIs and the IR absorption can be seen, but at about  $-250^\circ\text{CA}$ , ROI 2 starts to significantly lag the other locations and the IR absorption measurement. The lag with respect to the other ROIs persists until mid-compression. It is consistent with the expected flow in the upper center of the combustion chamber, where valve and tumble flows are expected to produce convection from left (ROI 3) to right (ROI 2) in both intake and compression stroke.

ROI 3, upstream of the sensor cage, best matches the IR absorption measurement during the rapid leaning around  $-240^\circ\text{CA}$ , with ROIs 2 and 4 having lower peaks than 1 and 3. In the case of ROI 2, this may be due to additional mixing in the wake of the sensor and spark electrode. The ratio of the

**FIGURE 13** Evolution of the relative air/fuel ratio  $\lambda$  from LIF imaging extracted from four different  $2.1 \times 2.1 \text{ mm}^2$  regions of interest (ROIs) surrounding the IR absorption sensor (red), compared to the results from the IR absorption measurement (all ensemble-averaged data). The locations of the ROIs and the color-coding of the corresponding traces are indicated in the inset.



20-cycle standard deviation and the mean value in ROI 1 at  $-220^\circ\text{CA}$  is 0.35. After intake-valve closes ( $-184^\circ\text{CA}$ ) and the in-cylinder flow presumably becomes much slower, ROI 4 yields very similar  $\lambda$  as ROIs 1 and 3, indicating that also in the immediate vicinity of the sensor the LIF imaging is not significantly affected by background. After  $-140^\circ\text{CA}$ ,  $\lambda$  from IR absorption is in between the values extracted from the different ROIs. At  $-40^\circ\text{CA}$  the ratio of the 20-cycle standard deviation and the mean value in ROI 1 is 0.11. Therefore, cyclic variability in the late compression stroke is lower than at  $-220^\circ\text{CA}$ , but still significant against the single-shot precision of the LIF measurements. Based on these results, we decided to average  $\lambda$  over ROI 1 to 3 and to use this mean value for the further comparisons. ROI 4, being farther away from the region of IR absorption measurements, was neglected. If CFD simulations are presented spatially averaged, also ROIs 1 to 3 are used.

Based on this spatial averaging around the spark plug sensor, Figure 14 compares the evolution of  $\lambda$  and temperature from LIF imaging and CFD simulation with that from the IR absorption sensor. The experimental results are ensemble-averaged. In addition, Figure 15 shows a field-wide comparison of  $\lambda$  from ensemble-averaged LIF imaging and from the CFD

**FIGURE 14** Comparison of  $\lambda$  and temperature from LIF imaging, IR absorption, and CFD simulation. LIF and CFD data were extracted from three ROIs around the spark plug sensor and then averaged. LIF data are taken from averages of 20 consecutive cycles, IR absorption from averages over three runs with 100 cycles each.

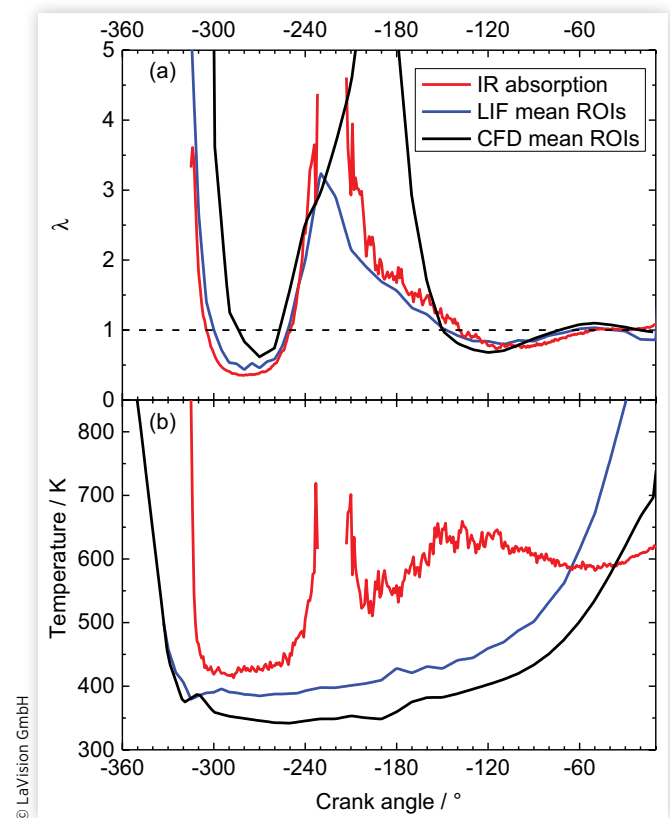
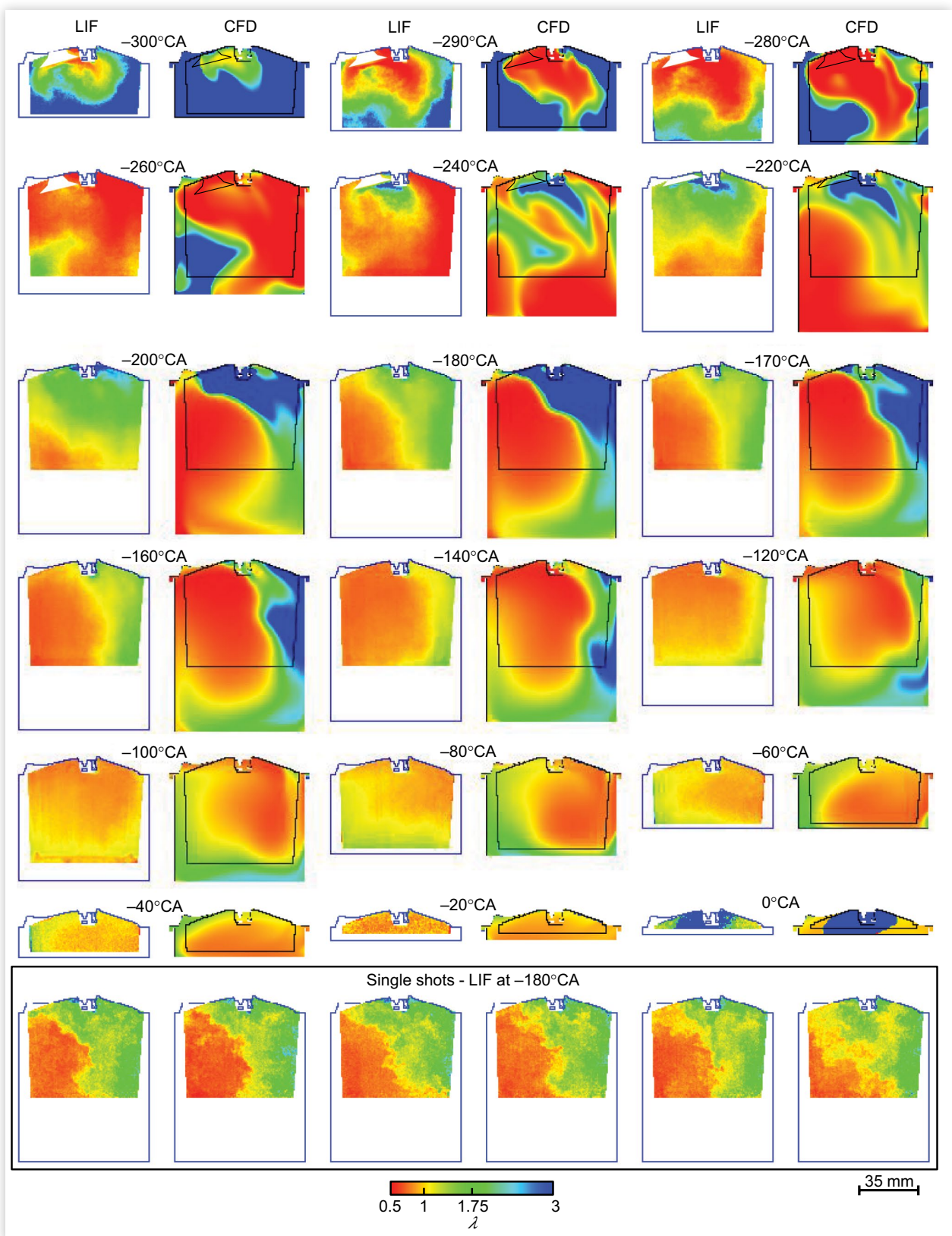


**FIGURE 15** Comparison of the  $\lambda$ -images as crank-angle evolution from LIF imaging and CFD simulation. LIF images at each crank angle are ensemble averages of 20 consecutive cycles. Also, single shot LIF  $\lambda$ -images of 6 consecutive cycles at  $-180^\circ\text{CA}$  are shown.



simulation for selected crank angles. Also, six single LIF shots from consecutive cycles at  $-180^\circ\text{CA}$  are shown to illustrate the cycle-to-cycle fluctuations. For orientation, the contour of the combustion chamber is indicated in the LIF-based images, and the LIF field of view in the CFD results. In LIF imaging, one of the open intake valves obscures parts of the field of view, while from the CFD information is available for the corresponding region.

Overall, in  $\lambda$  the two experiments and the simulation agree well. In particular, the spatio-temporal evolution from LIF imaging and the CFD simulation largely coincide. Both clearly show that in-cylinder mixture formation consists of clockwise tumble convection with gradual mixing. Figure 14 shows that the 3-region-average  $\lambda$  from the LIF data agrees well with the IR absorption measurement. In temperature, there are greater differences with significant disagreement at all crank angles.

At gas exchange TDC ( $-360^\circ\text{CA}$ ),  $\lambda$  is ill-defined, since apart from crevice outgassing only the products of stoichiometric combustion are present. From  $-330^\circ\text{CA}$  to  $-240^\circ\text{CA}$ , all methods yield qualitatively consistent  $\lambda$  showing the lean-rich-lean sequence during intake that already had been discussed with Figure 13. However, while LIF imaging and IR absorption agree in the timing of the fresh gas arriving at the probe volume, this event occurs about  $15^\circ\text{CA}$  later in the CFD. Figure 15 also shows this lag, but additionally it can be seen that the fresh charge penetrates into the cylinder faster in the CFD simulation, such that by  $-290^\circ\text{CA}$  the CFD is not lagging anymore. The initial offset may be due to inaccuracies in the CFD's domain geometry or the simulation itself in the intake pipe. In particular, there are some areas of flow detachment in the intake pipe that may not be captured accurately by this RANS-type simulation. The distance between injector and port is relatively long. Therefore, small differences in the calculated flow here can lead to the observed differences in the arrival time of the fuel at the valve. ( $15^\circ\text{CA}$  offset correspond to 7.5 mm distance at the mean pipe flow velocity.)

Figure 14 shows that between  $-240^\circ\text{CA}$  and  $-150^\circ\text{CA}$ , roughly corresponding to the lean phase of the intake flow, IR absorption and LIF imaging yield qualitatively similar results, with differences in maximum  $\lambda$ . Due to the very lean mixture, both experimental methods suffer from signals close to background at these crank angles, reducing the accuracy in  $\lambda$ , in addition to the differences caused by the locations of the sensor and the ROIs. CFD simulation, not affected by detection limits, predicts significantly larger  $\lambda$ , with the maximum ( $\lambda = 9.5$  at  $-190^\circ\text{CA}$ ) shifted by about  $+30^\circ\text{CA}$  with respect to the experimental techniques. The "falling edge" of the lean phase (high  $\lambda$  to low  $\lambda$ ) is much steeper in the CFD than it is in LIF imaging and IR absorption. This difference in temporal gradient (Figure 14) is consistent with the fact that the CFD simulation yields higher spatial gradients (Figure 15). The single-shot  $\lambda$  fields at the bottom of Figure 15 demonstrate that on an instantaneous basis, the gradients are in fact pronounced, but the CFD cannot capture the large-scale cyclic variability that smoothes out the ensemble mean, an effect that is well-known for RANS-type engine simulations [18, 29, 33].

During compression, beyond  $-150^\circ\text{CA}$ , Figure 14 shows  $\lambda$  given by all three techniques to be quite similar. Again, consistent with steeper spatial gradients, the slight lean-then-rich modulation during mid and late compression is stronger in the CFD. At ignition, the CFD simulation yields  $\lambda_{\text{CFD}} = 0.97$ , close to  $\lambda_{\text{global}} = 1$ , while IR absorption and LIF imaging yield  $\lambda_{\text{IR}} = 1.08$  and  $\lambda_{\text{LIF}} = 0.86$ , respectively. The actual value is unknown, but this is some indication that LIF may underestimate and IR absorption overestimate  $\lambda$ . A possible explanation for the latter is that residual gas was neglected in the data evaluation of the IR absorption measurement. The residual gas concentration was estimated by the gas-exchange model (see section "CFD simulation") to be 11%, reducing the amount of fresh air by a factor of 0.89. This can be applied to the IR absorption results by multiplication with the total gas density when calculating  $\lambda$ , resulting in  $\lambda_{\text{IR,corr}} = 0.95$  and thus close to the value from CFD. LIF imaging is, in first approximation, not influenced by residual gas since it directly measures the tracer/oxygen (i.e., fuel/air) ratio. However, in the LIF data evaluation, inaccuracies in the simultaneously measured temperature may propagate into  $\lambda$ .

In Figure 15 at TDC, the burnt area can be identified in LIF imaging by its local lack of signal. The direction of flame propagation is consistent with that predicted by the CFD simulation. Figure 15 shows the ensemble-averaged image, but because of the strong contrast between burnt and unburnt area, the burnt area is also clearly delineated in single shots.

In terms of temperature, Figure 14 shows that after  $-330^\circ\text{CA}$ , there is a nearly constant offset of about 50 K between LIF imaging and CFD simulation, increasing close to ignition. Since it is such a systematic deviation, it might originate from errors in the temperature calibration of the two-color LIF imaging. The heated-nozzle method described in section "Tracer-LIF imaging" for example does not take into account spectral changes with increasing pressure. However, underestimated wall temperatures in the boundary conditions of the CFD simulation might also contribute to the discrepancy. As discussed with Figure 11, the temperature from IR absorption exhibits a completely different evolution, because it is significantly influenced by heat exchange with the metal cage. Since temperature strongly influences the accuracy of the IR absorption method, the good agreement for  $\lambda$  between all methods is evidence that the temperature determined within the IR absorption path is reliable.

## Conclusions

We presented a comparison of two new optical techniques and a CFD simulation for analysis of mixture formation in CNG engines. Snapshot images of  $\lambda$  were computed from laser-induced fluorescence (LIF) imaging of anisole as a tracer added to the methane fuel. Simultaneously,  $\lambda$  was also derived from broadband infrared (IR) absorption over a short path in a spark-plug integrated sensor. The CFD simulation was performed with the RANS-approach and a commercial code,

including the protruding IR sensor in the domain with locally refined mesh resolution. All three methods are capable of determining  $\lambda$ , but they give complementary results. In the current implementation, LIF provides spatially resolved two-dimensional data on the mixture formation once per cycle. IR absorption is restricted to a point-like measurement, but at a high repetition rate delivering continuous crank-angle resolved measurements over consecutive cycles. The CFD simulation involves simplifying models of turbulence and mixing, but delivers three-dimensional results in all relevant scalars and velocity. In practical use, application of the IR absorption sensor in production engines is straightforward, whereas LIF is much more resource-intensive. The effort for CFD is in between, depending partly on what auxiliary models are already available to estimate the boundary conditions.

For both LIF imaging and IR absorption measurement, the temperature in the probe volume is a crucial auxiliary variable needed to determine  $\lambda$ . In both techniques, essentially the same approach was used, namely, exploiting a change of spectral features with temperature. This added experimental complexity but significantly improves accuracy. As a result, overall the two experiments and the simulation agree well in the measured or calculated  $\lambda$ . Visually, the spatio-temporal evolution from LIF imaging and the CFD simulation coincide very well. Both clearly show that in-cylinder mixture formation consists of clockwise tumble convection with gradual mixing. The CFD shows sharper spatial gradients, which is due to the RANS-approach. Sampled from around the spark-plug sensor in LIF images and CFD simulation, the crank-angle evolution of  $\lambda$  agrees well with the IR absorption measurement. The CFD simulation also agrees, except for an offset in the time at which the fuel-rich portion of the fresh gas enters. However, in temperature there is significant disagreement between the three methods at all crank angles. In particular, IR absorption yields a temperature evolution that is qualitatively different from LIF and CFD. With the additional spatial information available from the (LIF cross-checked) simulation, we conclusively showed that this temperature evolution is due to heat transfer of the spark-plug sensor's metal cage with the cylinder charge. It is "a feature, not a bug" and can be accounted for in data evaluation. Temperature from LIF imaging, however, is systematically about 50 K higher than that from the CFD simulation, which we could not attribute to any particular experimental issue.

The operating point investigated here is at low load. For the LIF imaging technique, to first order, higher load at the same equivalence ratio is inconsequential. The resulting higher wall and thus charge temperatures would be taken into account by the temperature correction, but signal and measurement precision would decrease somewhat. IR absorption becomes stronger with higher number density, but higher loads are limited by the heat resistance of the metal cage. In this case, a line-of-sight arrangement with optical access across the cylinder can be implemented, which is not limited in engine load as no parts protrude into the combustion chamber.

Further improvements of the IR absorption technique will include the investigation of other bandpass filter combinations,

and increasing the SNR. The use of two narrowband filters may lead to a more accurate determination of temperature. Including the measurement of residual-gas concentration through crank-angle resolved detection of CO<sub>2</sub> and H<sub>2</sub>O inside the measurement volume will also increase the accuracy of the derived  $\lambda$ .

In LIF imaging with a gaseous fuel, the main obstacle to better single-shot precision is the low tracer concentration. To increase the concentration, all elements of the fuel supply system would need to be heated, but with anisole already a modest temperature increase would greatly elevate the saturation vapor pressure. Precision could also be increased by choosing a different way of dealing with the temperature difference between motored calibration (flatfield) and fired measurements. For example, only the image-wide mean difference could be corrected for, since the spatially resolved temperature field is noisy. When there are no severe spatial temperature gradients, this trade-off of decreased accuracy for increased precision might be acceptable. Finally, although the absolute accuracy of the CFD simulation is not known, the systematic deviation of the LIF-based temperature from the CFD results may imply inaccuracies. A more accurate temperature would also make the LIF-deduced  $\lambda$  more accurate.

## Contact Information

### Sebastian Kaiser

University of Duisburg-Essen  
Institute for Combustion and Gas Dynamics  
Lotharstrasse 1, 47057 Duisburg, +49 203 379 1840  
[sebastian.kaiser@uni-due.de](mailto:sebastian.kaiser@uni-due.de)  
[www.uni-due.de/ivg/rf](http://www.uni-due.de/ivg/rf)

## Acknowledgments

This work was funded by the Federal Ministry of Education and Research (BMBF, Germany) within the project "OMeGAE", project IDs 13N13034, 13N13035, and 13N13036. We are thankful for the enthusiasm of the late Werner Hentschel in initiating this project. We also thank the colleagues from the departments Advance Development of SI Engines and Optical Measurements at VW.

## References

1. Nauwerck, A., Gindele, J., Spicher, U., Roskamp, H. et al., "Investigation of the Transient In-Cylinder Flow inside a Two Stroke Engine with Particle-Image-Velocimetry," SAE Technical Paper 2000-01-0902, 2000, doi:10.4271/2000-01-0902.
2. Gessenhardt, C., Schulz, C., and Kaiser, S.A., "Endoscopic Temperature Imaging in a Four-Cylinder IC Engine via Two-Color Toluene Fluorescence," *Proceedings of the Combustion Institute* 35(3):3697-3705, 2015, doi:10.1016/j.proci.2014.06.085.

3. Schulz, C. and Sick, V., "Tracer-LIF Diagnostics: Quantitative Measurement of Fuel Concentration, Temperature and Fuel/Air Ratio in Practical Combustion Systems," *Progress in Energy and Combustion Science* 31(1):75-121, 2005, doi:[10.1016/j.pecs.2004.08.002](https://doi.org/10.1016/j.pecs.2004.08.002).
4. Reboux, J., Puechberty, D., and Dionnet, F., "A New Approach of Planar Laser Induced Fluorescence Applied to Fuel/Air Ratio Measurement in the Compression Stroke of an Optical S.I. Engine," SAE Technical Paper [941988](https://doi.org/10.4271/941988), 1994, doi:[10.4271/941988](https://doi.org/10.4271/941988).
5. Sacadura, J.C., Robin, L., Dionnet, F., Gervais, D. et al., "Experimental Investigation of an Optical Direct Injection S.I. Engine Using Fuel-Air Ratio Laser Induced Fluorescence," SAE Technical Paper [2000-01-1794](https://doi.org/10.4271/2000-01-1794), 2000, doi:[10.4271/2000-01-1794](https://doi.org/10.4271/2000-01-1794).
6. Scholz, J., Wiersbinski, T., and Beushausen, V., "Planar Fuel-Air-Ratio-LIF with Gasoline for Dynamic Mixture-Formation Investigations," SAE Technical Paper [2007-01-0645](https://doi.org/10.4271/2007-01-0645), 2007, doi:[10.4271/2007-01-0645](https://doi.org/10.4271/2007-01-0645).
7. Sahoo, D., Petersen, B., and Miles, P.C., "Measurement of Equivalence Ratio in a Light-Duty Low Temperature Combustion Diesel Engine by Planar Laser Induced Fluorescence of a Fuel Tracer," *SAE Int. J. Engines* 4(2):2312-2325, 2011, doi:[10.4271/2011-24-0064](https://doi.org/10.4271/2011-24-0064).
8. Koban, W., Koch, J.D., Hanson, R.K., and Schulz, C., "Oxygen Quenching of Toluene Fluorescence at Elevated Temperatures," *Applied Physics B* 80(6):777-784, 2005, doi:[10.1007/s00340-005-1769-6](https://doi.org/10.1007/s00340-005-1769-6).
9. Koban, W., Koch, J.D., Hanson, R.K., and Schulz, C., "Absorption and Fluorescence of Toluene Vapor at Elevated Temperatures," *Physical Chemistry Chemical Physics* 6(11):2940-2945, 2004, doi:[10.1039/B400997E](https://doi.org/10.1039/B400997E).
10. Kaiser, S.A. and Long, M.B., "Quantitative Planar Laser-Induced Fluorescence of Naphthalenes as Fuel Tracers," *Proceedings of the Combustion Institute* 30(1):1555-1563, 2005, doi:[10.1016/j.proci.2004.08.263](https://doi.org/10.1016/j.proci.2004.08.263).
11. Rothamer, D.A., Snyder, J.A., Hanson, R.K., and Steeper, R.R., "Two-Wavelength PLIF Diagnostic for Temperature and Composition," *SAE Int. J. Fuels Lubr.* 1(1):520-533, 2008, doi:[10.4271/2008-01-1067](https://doi.org/10.4271/2008-01-1067).
12. Peterson, B., Baum, E., Böhm, B., Sick, V. et al., "Evaluation of Toluene LIF Thermometry Detection Strategies Applied in an Internal Combustion Engine," *Applied Physics B* 117(1):151-175, 2014, doi:[10.1007/s00340-014-5815-0](https://doi.org/10.1007/s00340-014-5815-0).
13. Lind, S., Retzer, U., Will, S., and Zigan, L., "Investigation of Mixture Formation in a Diesel Spray by Tracer-Based Laser-Induced Fluorescence Using 1-Methylnaphthalene," *Proceedings of the Combustion Institute* 36(3):4497-4504, 2017, doi:[10.1016/j.proci.2016.07.034](https://doi.org/10.1016/j.proci.2016.07.034).
14. Medaerts, F. and Puechberty, D., "In-Cylinder Fuel/Air Mixture and Flame Front Visualization in a Transparent Engine Using PLIF: A Comparison between Natural Gas and Gasoline Used as a Fuel," SAE Technical Paper [982524](https://doi.org/10.4271/982524), 1998, doi:[10.4271/982524](https://doi.org/10.4271/982524).
15. Rubas, P.J., Paul, M.A., Martin, G.C., Coverdill, R.E. et al., "Methane Jet Penetration in a Direct-Injection Natural Gas Engine," SAE Technical Paper [980143](https://doi.org/10.4271/980143), 1998, doi:[10.4271/980143](https://doi.org/10.4271/980143).
16. Salazar, V.M., Kaiser, S.A., and Halter, F., "Optimizing Precision and Accuracy of Quantitative PLIF of Acetone as a Tracer for Hydrogen Fuel," *SAE Int. J. Fuels Lubr.* 2(1):737-761, 2009, doi:[10.4271/2009-01-1534](https://doi.org/10.4271/2009-01-1534).
17. Salazar, V.M. and Kaiser, S.A., "Influence of the In-Cylinder Flow Field (Tumble) on the Fuel Distribution in a DI Hydrogen Engine Using a Single-Hole Injector," *SAE Int. J. Engines* 3(1):309-325, 2010, doi:[10.4271/2010-01-0579](https://doi.org/10.4271/2010-01-0579).
18. Scarcelli, R., Wallner, T., Matthias, N., Salazar, V. et al., "Mixture Formation in Direct Injection Hydrogen Engines: CFD and Optical Analysis of Single- and Multi-Hole Nozzles," *SAE Int. J. Engines* 4(2):2361-2375, 2011, doi:[10.4271/2011-24-0096](https://doi.org/10.4271/2011-24-0096).
19. Kirchweger, W., Haslacher, R., Hallmannsegger, M., and Gerke, U., "Applications of the LIF Method for the Diagnostics of the Combustion Process of Gas-IC-Engines," *Experiments in Fluids* 43(2-3):329-340, 2007, doi:[10.1007/s00348-007-0287-1](https://doi.org/10.1007/s00348-007-0287-1).
20. Friedrich, W., Grzeszik, R., and Wensing, M., "Mixture Formation in a CNG-DI Engine in Stratified Operation," SAE Technical Paper [2015-24-2474](https://doi.org/10.4271/2015-24-2474), 2015, doi:[10.4271/2015-24-2474](https://doi.org/10.4271/2015-24-2474).
21. Friedrich, W., Grzeszik, R., Helmich, M., Bossmeyer, T. et al., "Characterization of High Pressure Natural Gas Injections for Stratified Operation of a Spark Ignited Engine by Simultaneous Fuel Concentration and Air Entrainment Measurements," *18th International Symposium on the Application of Laser and Imaging Techniques to Fluid Mechanics*, Lisbon, Portugal, July 4-7, 2016.
22. Tomita, E., Kawahara, N., Nishiyama, A., and Shigenaga, M., "In Situ Measurement of Hydrocarbon Fuel Concentration near a Spark Plug in an Engine Cylinder Using the 3.392 Nm Infrared Laser Absorption Method: Application to an Actual Engine," *Measurement Science and Technology* 14(8):1357-1363, 2003, doi:[10.1088/0957-0233/14/8/322](https://doi.org/10.1088/0957-0233/14/8/322).
23. Grosch, A., Beushausen, V., Thiele, O., and Grzeszik, R., "Crank Angle Resolved Determination of Fuel Concentration and Air/Fuel Ratio in a SI-Internal Combustion Engine Using a Modified Optical Spark Plug," SAE Technical Paper [2007-01-0644](https://doi.org/10.4271/2007-01-0644), 2007, doi:[10.4271/2007-01-0644](https://doi.org/10.4271/2007-01-0644).
24. Witzel, O., Klein, A., Meffert, C., Wagner, S. et al., "VCSEL-Based, High-Speed, In Situ TDLAS for In-Cylinder Water Vapor Measurements in IC Engines," *Optics Express* 21(17):19951-19965, 2013, doi:[10.1364/oe.21.019951](https://doi.org/10.1364/oe.21.019951).
25. Witzel, O., Klein, A., Meffert, C., Schulz, C. et al., "Calibration-Free, High-Speed, In-Cylinder Laser Absorption Sensor for Cycle-Resolved, Absolute H<sub>2</sub>O Measurements in a Production IC Engine," *Proceedings of the Combustion Institute* 35(3):3653-3661, 2015, doi:[10.1016/j.proci.2014.06.038](https://doi.org/10.1016/j.proci.2014.06.038).
26. Grosch, A., Wackerbarth, H., Thiele, O., Berg, T. et al., "Infrared Spectroscopic Concentration Measurements of Carbon Dioxide and Gaseous Water in Harsh Environments with a Fiber Optical Sensor by Using the HITEMP Database," *Journal of Quantitative Spectroscopy and Radiative Transfer* 133:106-116, 2014, doi:[10.1016/j.jqsrt.2013.07.021](https://doi.org/10.1016/j.jqsrt.2013.07.021).

27. Bauke, S., Golibrzuch, K., Rotter, F., Wackerbarth, H. et al., "Quantitative, Time-Resolved Detection of CH<sub>4</sub> Concentrations in Flows for Injection Analysis in CNG Engines Using IR Absorption," *Journal of Sensors and Sensor Systems* 6(1):185-198, 2017, doi:[10.5194/jsss-6-185-2017](https://doi.org/10.5194/jsss-6-185-2017).
28. Golibrzuch, K., Digulla, F.-E., Bauke, S., Wackerbarth, H. et al., "Optical Sensor System for Time-Resolved Quantification of Methane Densities in CH<sub>4</sub>-Fueled Spark Ignition Engines," *Applied Optics* 56(22):6049-6058, 2017, doi:[10.1364/ao.56.006049](https://doi.org/10.1364/ao.56.006049).
29. Müller, F., Schmitt, M., Wright, Y.M., and Boulouchos, K., "Determination of Supersonic Inlet Boundaries for Gaseous Engines Based on Detailed RANS and LES Simulations," *SAE Int. J. Engines* 6(3):1532-1543, 2013, doi:[10.4271/2013-24-0004](https://doi.org/10.4271/2013-24-0004).
30. Seboldt, D., Lejsek, D., Wentsch, M., Chiodi, M. et al., "Numerical and Experimental Studies on Mixture Formation with an Outward-Opening Nozzle in a SI Engine with CNG-DI," SAE Technical Paper [2016-01-0801](https://doi.org/10.4271/2016-01-0801), 2016, doi:[10.4271/2016-01-0801](https://doi.org/10.4271/2016-01-0801).
31. Bartolucci, L., Scarcelli, R., Wallner, T., Swantek, A. et al., "CFD and X-Ray Analysis of Gaseous Direct Injection from an Outward Opening Injector," SAE Technical Paper [2016-01-0850](https://doi.org/10.4271/2016-01-0850), 2016, doi:[10.4271/2016-01-0850](https://doi.org/10.4271/2016-01-0850).
32. Deshmukh, A., Mayer, D., Bode, M. et al., "LES of Direct Gas Injection in Internal Combustion Engines," *LES for Internal Combustion Engine Flows*, Rueil-Malmaison, France, Nov. 30-Dec. 1, 2016.
33. Twellmeyer, A., Kopple, F., and Weigand, B., "Evaluating Different Measures to Improve the Numerical Simulation of the Mixture Formation in a Spark-Ignition CNG-DI-Engine," SAE Technical Paper [2017-01-0567](https://doi.org/10.4271/2017-01-0567), 2017, doi:[10.4271/2017-01-0567](https://doi.org/10.4271/2017-01-0567).
34. Tran, K.H., Guibert, P., Morin, C., Bonnetty, J. et al., "Temperature Measurements in a Rapid Compression Machine Using Anisole Planar Laser-Induced Fluorescence," *Combustion and Flame* 162(10):3960-3970, 2015, doi:[10.1016/j.combustflame.2015.07.033](https://doi.org/10.1016/j.combustflame.2015.07.033).
35. Shahbaz, M.A., Goschütz, M., and Kaiser, S.A., "Endoscopic Anisole-LIF Imaging of Flame Propagation and Temperature Fluctuations in a Production SI Engine," *8th European Combustion Meeting*, Dubrovnik, Croatia, Apr. 18-21, 2017.
36. Tran, K.H., Morin, C., Kühni, M., and Guibert, P., "Fluorescence Spectroscopy of Anisole at Elevated Temperatures and Pressures," *Applied Physics B* 115(4):461-470, 2014, doi:[10.1007/s00340-013-5626-8](https://doi.org/10.1007/s00340-013-5626-8).
37. Wang, Q., Tran, K.H., Morin, C., Bonnetty, J. et al., "Predicting Fluorescence Quantum Yield for Anisole at Elevated Temperatures and Pressures," *Applied Physics B* 123(7):199, 2017, doi:[10.1007/s00340-017-6773-0](https://doi.org/10.1007/s00340-017-6773-0).
38. Scholz, J., Röhl, M., Wiersbinski, T., and Beushausen, V., "Verification and Application of Fuel-Air-Ratio-LIF," *13th International Symposium on Applications of Laser Techniques to Fluid Mechanics*, Lisbon, Portugal, June 26-29, 2006.
39. Faust, S., Dreier, T., and Schulz, C., "Photo-Physical Properties of Anisole: Temperature, Pressure, and Bath Gas Composition Dependence of Fluorescence Spectra and Lifetimes," *Applied Physics B* 112(2):203-213, 2013, doi:[10.1007/s00340-013-5420-7](https://doi.org/10.1007/s00340-013-5420-7).
40. Zabeti, S., Aghsaei, M., Fikri, M., Welz, O. et al., "Optical Properties and Pyrolysis of Shock-Heated Gas-Phase Anisole," *Proceedings of the Combustion Institute* 36(3):4525-4532, 2017, doi:[10.1016/j.proci.2016.06.156](https://doi.org/10.1016/j.proci.2016.06.156).
41. Faust, S., Goschütz, M., Kaiser, S., Dreier, T. et al., "A Comparison of Selected Organic Tracers for Quantitative Scalar Imaging in the Gas Phase via Laser-Induced Fluorescence," *Applied Physics B* 117(1):183-194, 2014, doi:[10.1007/s00340-014-5818-x](https://doi.org/10.1007/s00340-014-5818-x).
42. Berrocal, E., Kristensson, E., Richter, M., Linne, M. et al., "Multiple Scattering Suppression in Planar Laser Imaging of Dense Sprays by Means of Structured Illumination," *Atomization and Sprays* 20(2):133-139, 2010, doi:[10.1615/AtomizSpr.v20.i2.30](https://doi.org/10.1615/AtomizSpr.v20.i2.30).
43. Berrocal, E., Kristensson, E., Hottenbach, P., Aldén, M. et al., "Quantitative Imaging of a Non-combusting Diesel Spray Using Structured Laser Illumination Planar Imaging," *Applied Physics B* 109(4):683-694, 2012, doi:[10.1007/s00340-012-5237-9](https://doi.org/10.1007/s00340-012-5237-9).
44. Mishra, Y.N., Kristensson, E., and Berrocal, E., "Reliable LIF/Mie Droplet Sizing in Sprays Using Structured Laser Illumination Planar Imaging," *Optics Express* 22(4):4480-4492, 2014, doi:[10.1364/OE.22.004480](https://doi.org/10.1364/OE.22.004480).
45. Mishra, Y.N., Kristensson, E., Koegl, M., Jönsson, J. et al., "Comparison between Two-Phase and One-Phase SLIPI for Instantaneous Imaging of Transient Sprays," *Experiments in Fluids* 58(9):2017, doi:[10.1007/s00348-017-2396-9](https://doi.org/10.1007/s00348-017-2396-9).
46. Rothman, L.S., Gordon, I.E., Babikov, Y. et al., "The HITRAN2012 Molecular Spectroscopic Database," *Journal of Quantitative Spectroscopy and Radiative Transfer* 130:4-50, 2013, doi:[10.1016/j.jqsrt.2013.07.002](https://doi.org/10.1016/j.jqsrt.2013.07.002).
47. Ferziger, J.H. and Perić, M., *Numerische Strömungsmechanik* First Edition (Berlin: Springer-Verlag, 2008), doi:[10.1007/978-3-540-68228-8](https://doi.org/10.1007/978-3-540-68228-8).
48. Peters, N., *Turbulent Combustion* First Edition (Cambridge University Press, 2000), doi:[10.1017/cbo9780511612701](https://doi.org/10.1017/cbo9780511612701).
49. Metghalchi, M. and Keck, J.C., "Burning Velocities of Mixtures of Air with Methanol, Isooctane, and Indolene at High Pressure and Temperature," *Combustion and Flame* 48:191-210, 1982, doi:[10.1016/0010-2180\(82\)90127-4](https://doi.org/10.1016/0010-2180(82)90127-4).
50. VECTIS User Manual (Version 2017.1b3), Computer Software, Ricardo, Inc., Belleville, MI, 2017.
51. Grosch, A., Beushausen, V., Wackerbarth, H., Thiele, O. et al., "Temperature- and Pressure-Dependent Midinfrared Absorption Cross Sections of Gaseous Hydrocarbons," *Applied Optics* 49(2):196-203, 2010, doi:[10.1364/AO.49.000196](https://doi.org/10.1364/AO.49.000196).